Screening-induced phase transitions in core-shell ferroic nanoparticles

Anna N. Morozovska ⬤,[1,*] Eugene A. Eliseev ⬤,[2] Yulian M. Vysochanskii ⬤,[3] Viktoria V. Khist,[4,5] and Dean R. Evans[6,†]

[1]*Institute of Physics, National Academy of Sciences of Ukraine, 46, pr. Nauky, 03028 Kyiv, Ukraine*
[2]*Institute for Problems of Materials Science, National Academy of Sciences of Ukraine, Krjijanovskogo 3, 03142 Kyiv, Ukraine*
[3]*Institute of Solid State Physics and Chemistry, Uzhhorod University, 88000 Uzhhorod, Ukraine*
[4]*Igor Sikorsky Kyiv Polytechnic Institute, 03056 Kyiv, Ukraine*
[5]*Institute of Magnetism, National Academy of Sciences of Ukraine, 03142 Kyiv, Ukraine*
[6]*Air Force Research Laboratory, Materials and Manufacturing Directorate, Wright-Patterson Air Force Base, Ohio 45433, USA*

Using the Landau-Ginzburg-Devonshire approach, we study screening-induced phase transitions in core-shell ferroic nanoparticles for three different shapes: an oblate disk, a sphere, and a prolate needle. The nanoparticle is made of a ferroic $CuInP_2S_6$ core and covered by a tunable screening shell made of a phase-change material with a conductivity that varies as the material changes between semiconductor and metallic phases. We reveal a critical influence of the shell screening length on the phase transitions and spontaneous polarization of the nanoparticle core. Since the tunable screening shell allows the control of the polar state and phase diagrams of core-shell ferroic nanoparticles, the obtained results can be of particular interest for applications in nonvolatile memory cells.

I. INTRODUCTION

The role of the surface state increases significantly with a decrease in the size of nanoscale ferroics, often leading to size-induced phase transitions [1,2], which can result in unusual polarization dynamics and morphology of polar domains related to surface screening [3,4]. Surface screening becomes especially important in recently discovered nanoscale Cu-based layered chalcogenides, $CuInP_2(S, Se)_6$ [5–7], which are uniaxial ferroics [8–10] with a possibility of the ferrielectricity and antiferrielectricity downscaling to the limit of a single layer [11,12]. Ferrielectricity, the equivalent of ferrimagnetism, can be termed as an antiferroelectric order but with a switchable spontaneous polarization created by two sublattices with spontaneous dipole moments that are antiparallel and different in magnitude [13,14]. From a microscopic point of view, $CuInP_2(S, Se)_6$ nanoparticles are ferrielectrics (FIs) [13]; the macroscopic spontaneous polarization of $CuInP_2S_6$ (CIPS) ranges from 0.03 to 0.12 C/m^2 [15], while for $CuInP_2Se_6$, it is ~0.025 C/m^2 [16]. The spontaneous polarization occurs at ~(310–320) K for CIPS and at ~230 K for $CuInP_2Se_6$ [17,18]. The $CuInP_2(S, Se)_6$ family reveals very unusual features: a nonlinear dielectric response, indicating that a spontaneous polarization may exist above the FI transition temperature [19]; extremely large elastic nonlinearity in the [001] direction perpendicular to the layers [20,21]; giant negative electrostriction; giant piezoelectricity; and dielectric tunability [22]. Of great interest are electrostriction-induced piezoelectricity above the

FI transition temperature [23], morphotropic phase transitions between the monoclinic and trigonal phases [24], anomalous bright domain walls with an enhanced local piezoelectric response [25,26], and giant flexoelectric response [12].

Despite the significant fundamental and practical interest in nanoscale $CuInP_2(S, Se)_6$, the influence of surface screening on their phase diagrams and polar properties are poorly studied. Here, very interesting effects can be expected in $CuInP_2(S, Se)_6$ nanoparticles covered by tunable shells; this expectation is based on our previous studies of stress-induced phase transitions in CIPS ellipsoidal nanoparticles [27] and predictions of unusual polar states in other core-shell nanoparticles. We simulated unusual labyrinthine patterns [28,29], vortices with kernels [30,31], twisted vortices [32], and meronlike flexons [33] in a spherical (or cylindrical) ferroelectric core covered with a tunable paraelectric (PE) shell placed in a soft polymer (or liquid medium). Labyrinthine domains can exist in spherical core-shell nanoparticles with a uniaxial FI CIPS or ferroelectric $Sn_2P_2S_6$ core and may have a quasi-infinite number of equal-energy states [28,29]. Vortex states with a kernel may occur in spherical core-shell nanoparticles with a multiaxial ferroelectric $BaTiO_3$ or $BiFeO_3$ core, which possess a manifold degeneracy [30–32]. The great number of the equal-energy domain states may be the reason for a low-frequency negative susceptibility [34].

Using the four-well Landau-Ginzburg-Devonshire (LGD) thermodynamic potential reconstructed in Ref. [27], we study the screening-induced phase transitions in core-shell nanoparticles, whose shape varies, i.e., a prolate needle, an oblate disk, or a sphere. The nanoparticle core is made of CIPS. This paper briefly discusses basic expressions of the LGD approach (Sec. II) and considers in detail the screening-induced phase transitions and polarization changes in these core-shell

———————
*anna.n.morozovska@gmail.com
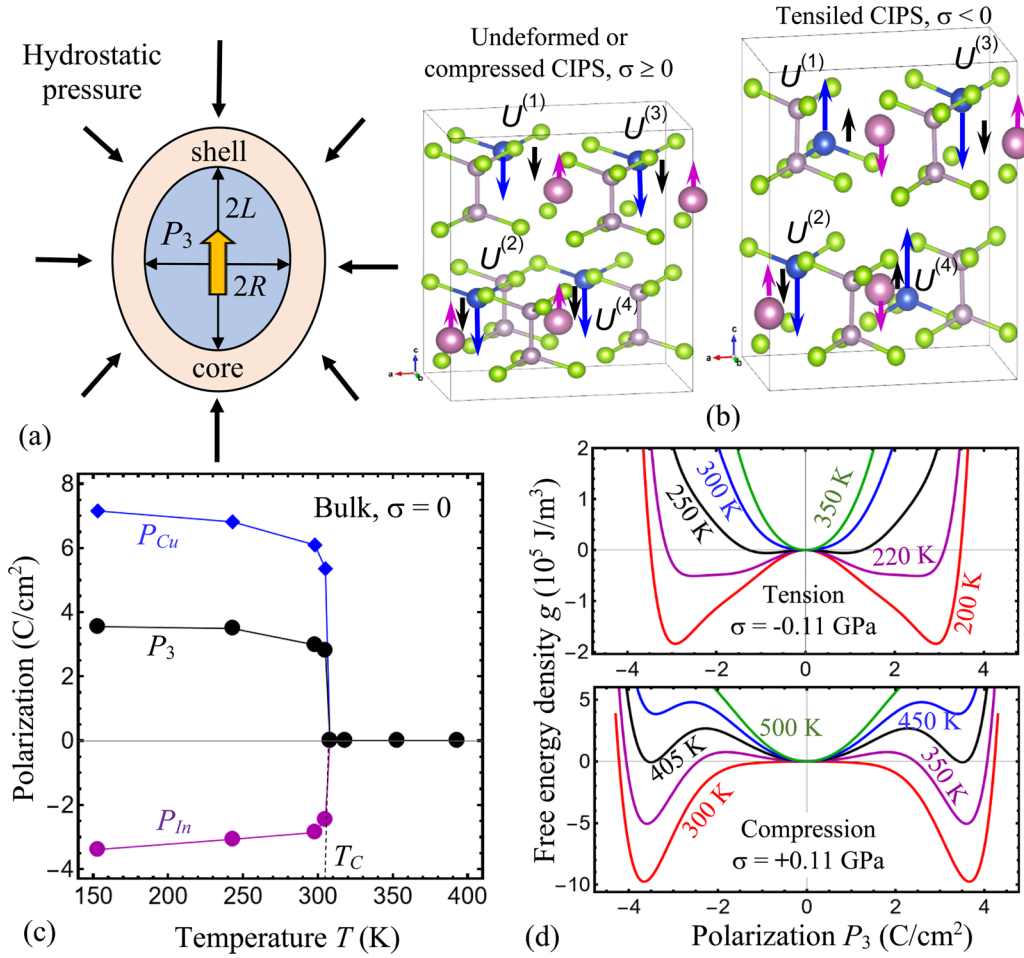†dean.evans@afrl.af.mil

FIG. 1. (a) Core-shell nanoellipsoid with semi-axes R and L. The thick orange arrow shows the spontaneous polarization directed along the ellipsoidal axis L; thin black arrows illustrate the direction of the hydrostatic pressure application (compression is depicted in the schematic). (b) Atomic structure of CIPS [25], where the blue, large violet, small gray-violet, and yellow balls are Cu, In, P, and S atoms, respectively. Violet and blue arrows schematically illustrate the opposite dipole moments of In and Cu sublattices, respectively. Black arrows are resulting polar displacements $U^{(m)}$ in two ferrielectric (FI) states with large (left structure) and zero (right structure) total polarizations. The orientation of crystallographic axes a, b, and c is shown at the bottom of each structure. (c) Temperature dependence of polarizations created by individual Cu and In dipoles in the FI phase and the resulting net polarization P_3. Symbols are experimental data from Fig. 4(a) in Ref. [13]; blue, black, and violet solid curves are theoretical fitting for a bulk CIPS at $\sigma = 0$. (d) Typical dependences of the free energy on polarization P_3 calculated for a bulk CIPS at negative (top plot) and positive hydrostatic pressures $\sigma = -0.11$ GPa (top plot) and $\sigma = +0.11$ GPa (bottom plot). Red, violet, black, blue, and green curves correspond to different temperatures T from 200 to 500 K.

nanoparticles (Sec. IV). Section V provides conclusions of the results.

II. PROBLEM FORMULATION

A core-shell nanoellipsoid with semi-axes R and L is shown in Fig. 1(a). The spontaneous polarization of the CIPS core P_3 is directed along the ellipsoid semi-axis L. The macroscopic polarization P_3 is the total polarization of four possible polar-active sublattices $U_3^{(i)}$, $P_3 = \frac{e}{2}[U_3^{(1)} + U_3^{(2)} + U_3^{(3)} + U_3^{(4)}]$ (see Fig. 1(b) and eq. (2a) in Ref. [26]), in which individual dipole moments of the four Cu and four In atoms are antiparallel and different in magnitude in the absence of an external electric field and applied pressure. Polarizations created by individual Cu and In dipoles and resulting polarization P_3 are shown in Fig. 1(c), where we use experimental data from Fig. 4(a) in Ref. [13]. The polarization

P_3 is a polar long-range order parameter, which can be directly determined by ferroelectric measurements and piezoelectric response microscopy. The antipolar order parameter A_3 is defined as one of three possible half-differences of the sublattices polarizations, e.g., $A_3 = \frac{e}{2}[U_3^{(1)} - U_3^{(2)} - U_3^{(3)} + U_3^{(4)}]$ (see Eq. (2b) in Ref. [26]). The antipolar order parameters cannot be directly measured in the abovementioned experiments. Indirectly, the nonlinear coupling between A_3 and P_3 increases the order of the thermodynamic potential G (e.g., Gibbs free energy), describing the polar behavior of CIPS (see Appendix A for details).

It has been shown [27] that CIPS free energy $G(P_3)$ can have one potential well at $P_3 = 0$, three wells at $P_3 = 0$ and $P_3 = \pm P_{S1}$, two wells at $P_3 = \pm P_{S2}$, two plateaus at $P_{S2} \leqslant |P_3| \leqslant P_{S1}$, or four wells at $P_3 = \pm P_{S2}$ and $P_3 \approx \pm P_{S1}$; Gibbs free energy is dependent on the value of applied hydrostatic pressure σ and temperature T.

Typical dependences of the CIPS free energy density g on polarization P_3 calculated for $\sigma < 0$ and $\sigma > 0$ for different values of T are shown in Fig. 1(d). The PE-FI phase transition is of the second order for the tension of the CIPS lattice [see the top plot in Fig. 1(d), where $\sigma < 0$]. The second-order scenario is realized because the distance between the sublattices increases and interaction between the layers becomes weaker in the tensile lattice. As a result, the long-range electrostatic interaction between the sublattice dipoles becomes weaker, and so their antiparallel ordering in the four sublattices becomes favorable to minimize the electrostatic energy of dipole-dipole interactions [small black arrows are antiparallel in the right atomic structure of Fig. 1(b)]. This in turn provides a local antiferroelectric state, where $P_3 = 0$ and $A_3 \neq 0$ can occur in a given unit cell, consisting of four sublattices (see, e.g., three possible antiferroelectric orderings in Figs. 1(b)–1(d) in Ref. [26]). In accordance with *ab initio* calculations and earlier results [27], the local antiferroelectric orderings [such as shown in the right Fig. 1(b)] mix with local FI ordering [such as shown in the left side of Fig. 1(b)]. As a result, a small spontaneous polarization $P_3 = \pm P_{S2}$ arises continuously with the temperature decreasing below T_C [see the appearance and deepening of two relatively shallow potential wells in the top plot of Fig. 1(d)].

The PE-FI phase transition is of the first order for the undeformed and compressed CIPS lattice [see the bottom plot in Fig. 1(d), where $\sigma > 0$]. The first-order scenario exists because the distance between the sublattices is flawed in the compressed lattice. As a result, the long-range electrostatic interaction between the sublattice dipoles becomes stronger, and so their parallel ordering in the four sublattices becomes favorable to minimize the electrostatic energy of dipole-dipole interactions [small black arrows are parallel in the left atomic structure of Fig. 1(c)]. This results in a large spontaneous polarization $P_3 = \pm P_{S1}$, which arises sharply below T_C [see the formation and deepening of two relatively deep potential wells separated by potential barrier in the bottom plot of Fig. 1(d)].

Note that any type of mechanical action (e.g., hydrostatic pressure, biaxial or uniaxial mechanical strain or stress) can change the nanoparticle polar state due to the electrostriction effect [27]. Due to the strong electrostrictive coupling, a strain on the order of a few percent (± 0.5 to $\pm 1.5\%$) significantly influences the phase diagram, spontaneous polarization, and dielectric properties of ferroelectric perovskite films [35]. The influence of relatively small biaxial strains ($\sim \pm 0.5\%$) on a free energy landscape, phase diagrams, and P_3 value appears very strong in CIPS films (see, e.g., Fig. 4 in Ref. [27]). A few percent compressive or tensile strains are more than enough to switch CIPS between nonpolar ($P_3 = 0$, $A_3 = 0$), antipolar ($P_3 = 0$, $A_3 \neq 0$), and polar ($P_3 \neq 0$, $A_3 = 0$) states [compare, e.g., the blue parabolic curve in the top plot in Fig. 1(d) with the red double-well curve in the bottom plot in Fig. 1(d), where $T = 300$ K, $\sigma = -0.11$ GPa (top plot), and $\sigma = +0.11$ GPa (bottom plot)].

The core is covered by a tunable screening shell made of a phase-change material, whose electric conductivity varies as the material changes between semiconductor and metallic phases. The metallic state shell with a greater conductivity corresponds to a very small effective screening length $\lambda <$ 0.05 nm, which screens the depolarization electric field, supports the spontaneous polarization of the core, and can prevent domain splitting in the core. The semiconductor state shell with a relatively weaker conductivity corresponds to a larger screening length $\lambda > 0.5$ nm, resulting in a decrease of the core polarization and a possible appearance of domain splitting to minimize the electrostatic energy of the depolarization field in the system.

In Appendix A, we have shown that the Landau-Devonshire expansion G in even (second, fourth, and sixth) powers of the polar order parameter (P_3) and the antipolar order parameter (A_3) after partial minimization $\frac{\partial G}{\partial A_3} = 0$ can be transformed to the expansion in even powers (second, fourth, sixth, and eighth) of the polarization P_3. The density of the four-well LGD potential g_{LGD}, which includes the Landau-Devonshire expansion in even powers of the polarization P_3 up to the eighth power g_{LD}, the Ginzburg gradient energy g_G, and the elastic and electrostriction energies g_{ES}, has the form [27]:

$$g_{LGD} = g_{LD} + g_G + g_{ES}, \tag{1a}$$

$$g_{LD} = \frac{\alpha^*}{2}P_3^2 + \frac{\beta}{4}P_3^4 + \frac{\gamma}{6}P_3^6 + \frac{\delta}{8}P_3^8 - P_3 E_3, \tag{1b}$$

$$g_G = g_{33ij}\frac{\partial P_3}{\partial x_i}\frac{\partial P_3}{\partial x_j}, \tag{1c}$$

$$g_{ES} = -\frac{s_{ij}}{2}\sigma_i\sigma_j - Q_{i3}\sigma_i P_3^2 - Z_{i33}\sigma_i P_3^4 - W_{ij3}\sigma_i\sigma_j P_3^2. \tag{1d}$$

In accordance with LGD theory, the coefficients β, γ, and δ in Eq. (1b) are temperature independent. The values σ_i denote diagonal components of a stress tensor in the Voigt notation, and a subscript $i = 1$–6. The values Q_{i3}, Z_{i33}, and W_{ij3} denote the components of a single linear and two nonlinear electrostriction strain tensors, respectively [36,37]. Here, E_3 is an electric field component codirected with the polarization P_3.

The strength and anisotropy of the polarization gradient energy are defined by the tensor g_{33ij}. As it has been shown earlier [28], the critical sizes of the CIPS core corresponding to the ferroelectric-PE phase transition, as well as the domain structure appearance and its morphology in the ferroelectric state, depend strongly on the magnitude and anisotropy of the polarization gradient coefficients g_{33ij}. An order of magnitude increase in g_{33ij} (e.g., $>10^{-9}$ J m^3 C^{-2}) leads to a relatively small increase of the critical sizes (less than several nanometers), but it strongly suppresses the domain structure appearance in the ferroelectric state. For instance, in the case $g \cong 2 \times 10^{-9}$ J m^3 C^{-2} (used in this paper, see Table I), CIPS nanoparticles are mostly single domain above the critical sizes and PE below the critical sizes. In addition, for the case of natural boundary conditions $g_{33ij}n_i\frac{\partial P_3}{\partial x_j} = 0$, also used in this paper, polarization gradient effects can be neglected in the single-domain state.

To focus on the influence of external pressure, we neglect the surface tension considered elsewhere [2,29,38]. We also would like to underline that we consider only hydrostatic pressure $\sigma_1 = \sigma_2 = \sigma_3 = \sigma$ in this paper since the pressure is the easiest to realize experimentally for an ensemble of

TABLE I. LGD parameters for a bulk FI CIPS.

Coefficient	Value
ε_b	9
α_T (C^{-2} m J K^{-1})	1.64067×10^7
T_C (K)	292.67
β (C^{-4} m^5 J)	3.148×10^{12}
γ (C^{-6} m^9 J)	-1.0776×10^{16}
δ (C^{-8} m^{13} J)	7.6318×10^{18}
Q_{i3} (C^{-2} m^4)	$Q_{13} = 1.70136 - 0.00363\,T$,
	$Q_{23} = 1.13424 - 0.00242\,T$,
	$Q_{33} = -5.622 + 0.0105\,T$
Z_{i33} (C^{-4} m^8)	$Z_{133} = -2059.65 + 0.8\,T$,
	$Z_{233} = -1211.26 + 0.45\,T$,
	$Z_{333} = 1381.37 - 12\,T$
W_{ij3} (C^{-2} m^4 Pa^{-1})	$W_{113} \approx W_{223} \approx W_{333} \cong -2 \times 10^{-12}$
s_{ij} (Pa^{-1})	$s_{11} = 1.510 \times 10^{-11}$, $s_{12} = 0.183 \times 10^{-11}$
g_{33ij} (J m^3 C^{-2})	$g \cong 2 \times 10^{-9}$

nanoparticles. It is seen from Eq. (1d) that $g_{ES}(\sigma) \neq g_{ES}(-\sigma)$ due to the terms $\sigma_i(Q_{i3}P_3^2 + Z_{i33}P_3^4)$; therefore, the influence of the compression ($\sigma > 0$) and expansion ($\sigma < 0$) on the phase diagrams and polar properties of ferroelectrics can be vastly different [35].

In Eq. (1b), the temperature-, shape-, size-, and screening-dependent function α^* is introduced [27]:

$$\alpha^*(T, n_d, \Lambda) = \alpha(T) + \frac{n_d}{\varepsilon_0[\varepsilon_b n_d + \varepsilon_s(1 - n_d) + n_d \Lambda]}. \quad (2)$$

Here, the coefficient α depends linearly on the temperature T, $\alpha(T) = \alpha_T(T - T_C)$, where T_C is the Curie temperature of the bulk FI. The derivation of Eq. (2) is given in Ref. [39]. The dimensionless parameter n_d is the shape-dependent depolarization factor introduced as [40]

$$n_d(\zeta) = \frac{1 - \xi^2}{\xi^3}\left(\ln\sqrt{\frac{1+\xi}{1-\xi}} - \xi\right),$$

$$\xi(\zeta) = \sqrt{1 - \zeta^2}, \quad \zeta = \frac{R}{L}. \quad (3)$$

Here, ξ is the eccentricity ratio of the ellipsoid with semi-axes R and L, and ζ is the dimensionless shape factor. Parameters ε_b and ε_s are the background dielectric permittivity [41] of the FI core and the relative dielectric permittivity of the shell, respectively. The dimensionless screening factor Λ is introduced as

$$\Lambda = \frac{\lambda}{L}. \quad (4)$$

Let us consider nanoparticles with a small size $L < 10$ nm. In this case, small screening factors $\Lambda < 0.01$ correspond to a high screening degree provided by the conducting (i.e., metallic and semimetallic) state of the phase-change tunable shell. Larger screening factors $0.1 < \Lambda < 1$ correspond to a low screening degree provided by the semiconducting state of the tunable shell.

The values of T_C, α_T, β, γ, δ, Q_{i3}, and Z_{i33} have been determined in Refs. [26,27] from the fitting of temperature-

dependent experimental data for the dielectric permittivity [42–44], spontaneous polarization [13], and lattice constants [10] as a function of hydrostatic pressure. Elastic compliances s_{ij} were estimated from ultrasound velocity measurements [21,23,45]. The details for determining the CIPS material parameters are given in the supplement of Ref. [27]. Unfortunately, we did not find a full set of reliable experimental data for CIPS that would allow us to determine all nonlinear electrostriction coefficients W_{ijk} with satisfactory accuracy. However, we managed to estimate the diagonal components W_{ii3}, which are coupled with the hydrostatic pressure in Eq. (1d), using the experimental results in Ref. [46]. The gradient coefficients g_{33ij} are not determined in Refs. [26,27] but estimated from the width of domain walls. The CIPS parameters are listed in Table I.

Note that the phenomenological LGD approach used in this paper includes the electrostrictive coupling between the polar order parameter P_3 and elastic stresses (or strains) via Eq. (1d), where the components of linear (Q_{i3}) and nonlinear (Z_{i33} and W_{ij3}) electrostrictive tensors have been have been determined (or at least estimated) from experimental results for CIPS. They are listed in Table I. To the best of our knowledge, the situation with the estimates of anti-electrostrictive coupling in CIPS, which can be written as $g_{AES} = -\tilde{Q}_{i3}\sigma_i A_3^2 - \tilde{Z}_{i33}\sigma_i A_3^4 - \tilde{W}_{ij3}\sigma_i\sigma_j A_3^2$, as well with cross-terms, such as $\tilde{R}_{i3}\sigma_i A_3 P_3$, is unresolved because A_3 cannot be directly observed, and the components of tensors $\tilde{Q}_{i3}$, $\tilde{Z}_{i33}$, $\tilde{W}_{ij3}$, and $\tilde{R}_{i3}$ are unknown. Because of this, many authors (including this paper) do not consider the anti-electrostrictive coupling terms, which are regarded negligibly small. However, we realize that these terms can be important, and it is desirable to estimate them from, e.g., density functional theory calculations, for future considerations.

III. METHODS

For constructing phase diagrams, we found the minima of free energy numerically, as a function of several variables (e.g., the temperature, sizes, and/or the screening length), and calculated the equilibrium values of the polarization in the minima. Whenever it was possible, we used analytical expressions for phase boundaries (e.g., for the stability of the PE phase), and superimposed corresponding curves on the color maps of polarization. Numerical results presented in this paper are obtained and visualized using a specialized software, Mathematica 12.2 [47], and the Mathematica notebook, which contains the codes, is available at Ref. [48].

IV. SCREENING-INDUCED PHASE TRANSITIONS IN CORE-SHELL NANOPARTICLES

Here, we account for the effect of the hydrostatic pressure σ on the spontaneous polarization and phase diagram of the core-shell nanoparticles. The phase diagram in Fig. 2(a) illustrates the typical influence of the hydrostatic pressure on the polar state of an ellipsoidal CIPS nanoparticle. It contains a large dark-violet region representing the PE phase that expands toward higher temperatures and a region of the FI phase,
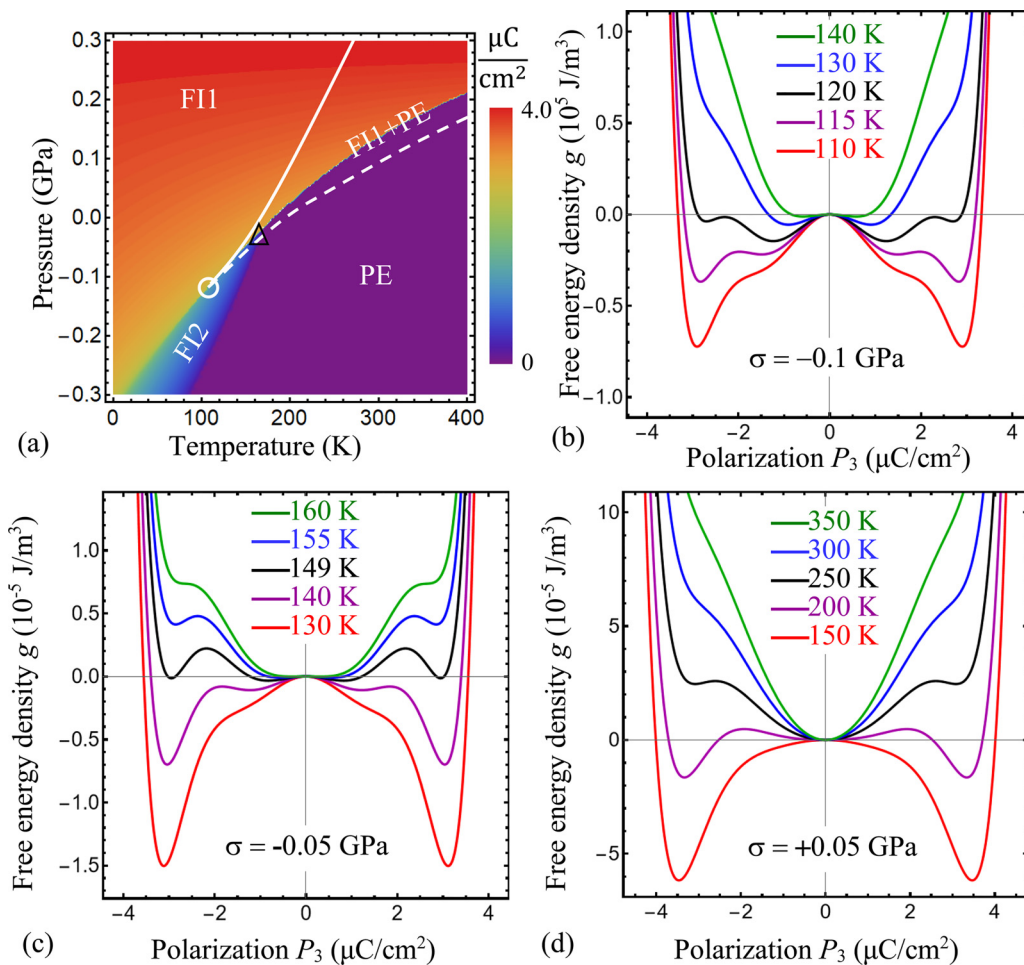
FIG. 2. (a) The dependence of the spontaneous polarization P_3 on temperature and pressure calculated for the stressed CIPS nanoellipsoid with semi-axes $R = 10$ nm and $L = 20$ nm. White solid and dashed curves are the absolute instabilities of the boundaries of the paraelectric (PE) and ferrielectric (FI) phases, respectively. A critical endpoint is marked by a black triangle, and a bicritical endpoint is marked by a white circle (see explanation in the text). The dependences of the free energy on polarization P_3 calculated for the hydrostatic pressures (b) $\sigma = -0.1$ GPa, (c) $\sigma = -0.05$ GPa, and (d) $\sigma = +0.05$ GPa. Red, violet, black, blue, and green curves correspond to different temperatures T from 110 to 350 K (see legends). The effective screening length $\lambda = 0.5$ nm and permittivity $\varepsilon_e = 2$; other CIPS parameters are listed in Table I.

which has two states. A smaller reddish region represents the FI state 1 (abbreviated as FI1) with a relatively large polarization P_3 that corresponds to the compression of the particle ($\sigma > 0$), and a small bluish region of the FI state 2 (abbreviated as FI2) with a small P_3 corresponds to the particle expansion under tension ($\sigma < 0$). The phase diagram has a critical endpoint (CEP), marked by a black triangle and located at $\sigma_{CEP} \approx -0.05$ GPa and $T_{CEP} \approx 180$ K, and a bicritical endpoint (BEP) [27,49], marked by a white circle and located at $\sigma_{BEP} \approx -0.11$ GPa and $T_{BEP} \approx 100$ K. The dependences of the free energy g_{LGD} on the polarization P_3 calculated for different pressures and temperatures are shown in Figs. 2(b)–2(d).

Phase diagrams and the FI-PE transition order depend on pressure due to the electrostriction coupling terms $-Q_{i3}\sigma_i P_3^2 - Z_{i33}\sigma_i P_3^4 - W_{ij3}\sigma_i\sigma_j P_3^2$, in Eq. (1d). The coupling changes the coefficients $\frac{\alpha^*}{2}$ and $\frac{\beta}{4}$ in the Landau-Devonshire energy Eq. (1b) to $(\frac{\alpha^*}{2} - Q_{i3}\sigma_i - W_{ij3}\sigma_i\sigma_j)$ and $(\frac{\beta}{4} - Z_{i33}\sigma_i)$, respectively. Since $\beta > 0$, $\gamma < 0$, and $\delta > 0$, the pressure σ_{cr} and temperature T_{cr}, which correspond to the BEP, are

determined from the conditions [27]:

$$(Z_{133} + Z_{233} + Z_{333})\sigma_{cr} = \frac{1}{4}\left(\beta - \frac{\gamma^2}{3\delta}\right), \quad (5a)$$

$$\alpha_T(T_{cr} - T_C) = 2\sigma_{cr}(Z_{133} + Z_{233} + Z_{333})$$
$$+ 2(W_{113} + W_{223} + W_{333})\sigma_{cr}^2$$
$$+ \frac{\gamma^3}{27\delta^2}, \quad (5b)$$

where Q_{i3} and Z_{i33} linearly depend on T. Due to the terms $\frac{\gamma}{6}P_3^6 + \frac{\delta}{8}P_3^8$, negative nonlinear electrostriction couplings $Z_{i33} < 0$ and $W_{ij3} < 0$, and the inverted signs of the linear electrostriction coupling $Q_{33} < 0$, $Q_{23} > 0$, and $Q_{13} > 0$ for CIPS, the pressure effect on the phase diagram is complex and unusual [27].

At $\sigma < \sigma_{CEP}$ the second-order FI-PE transition occurs through the FI2 state with a diffuse boundary [see the green diffuse boundary in Fig. 2(a) and the dependences of g_{LGD} on P_3 in Fig. 2(b)]. The diffuseness means that the spontaneous
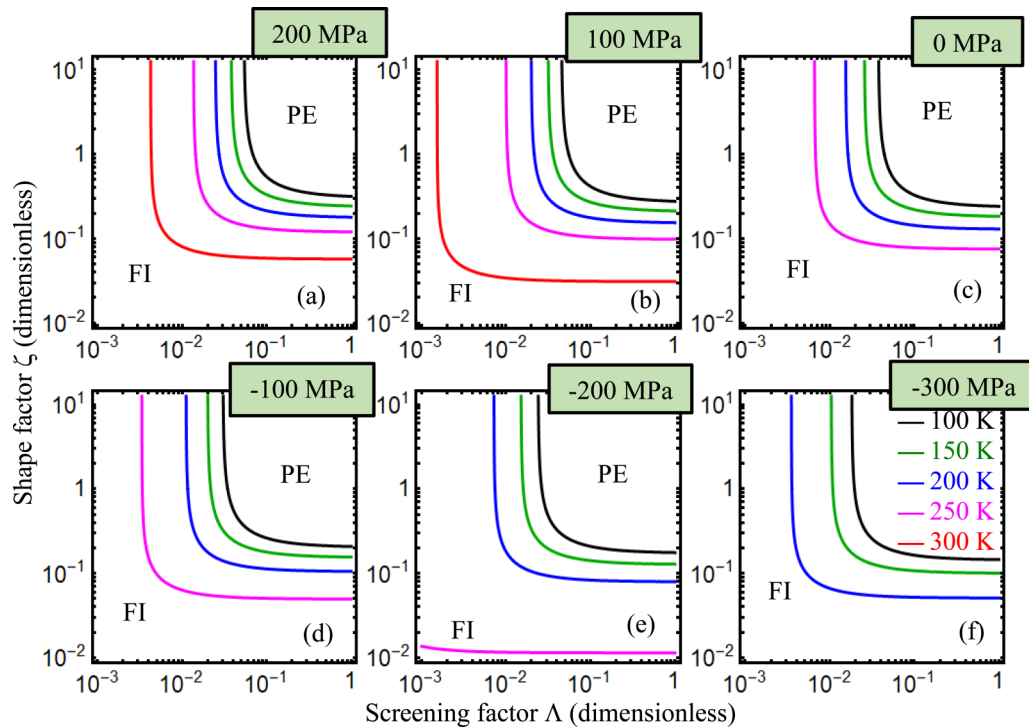
FIG. 3. Phase diagrams of the core-shell CIPS nanoparticles and their dependence on the screening factor Λ and shape factor ζ. The diagrams are calculated for different temperatures $T = 100, 150, 200, 250,$ and 300 K (black, green, blue, magenta, and red curves, respectively), and hydrostatic pressures (a) $\sigma = 200$ MPa, (b) 100 MPa, (c) 0 MPa, (d) -100 MPa, (e) -200 MPa, and (f) -300 MPa.

polarization changes continuously from zero to nonzero values inside the FI2 state. The FI-PE second-order transition line at CEP meets the FI-PE first-order transition line. At $\sigma < \sigma_{\text{CEP}}$, the first-order transition line is in the FI phase, and a sharp increase of the P_3 value is observed at this line. The magnitude of this increase from a small P_3 value in the FI2 state to a large P_3 value in the FI1 state decreases with an increase of tensile stress, until the stress and temperature values approach the BEP (note BEP is characterized by $\sigma_{\text{BEP}} \approx -0.11$ GPa and $T_{\text{BEP}} \approx 100$ K). At $\sigma < \sigma_{\text{BEP}}$, a second-order transition occurs, resulting in a continuous increase of the P_3 when moving from the FI2 to the FI1 state.

At $\sigma > \sigma_{\text{CEP}}$, the first-order FI-PE transition appears in the region of coexisting PE phase and FI1 state (abbreviated as FI1 + PE), where the FI1 state is stable and the PE phase is metastable. The spontaneous polarization has a steep drop at the PE phase boundary [see the sharp reddish-violet boundary between the PE and FI1 + PE regions in Fig. 2(a) and the dependences of g_{LGD} on P_3 in Figs. 2(c) and 2(d)].

The coexistence of the FI and PE phases occurs around the first-order transition, and the coexisting region expands with a positive pressure increase (see Ref. [27] for details). The white solid and dashed curve position is not seen on the color scheme because the numerical algorithm calculates the value of the spontaneous polarization only and cannot estimate the ratio of the FI1 to PE clusters. The FI1 + PE region in Fig. 2(a) is the color map of the spontaneous polarization but not the average polarization of FI1 and PE clusters in the region. The white solid curve, which separates the FI1 and FI1 + PE regions, corresponds to a complete disappearance of the

metastable potential well at $P_3 = 0$ and is always inside the FI1 region. The white dashed curve corresponds to a complete disappearance of the metastable potential well at $P_3 = \pm P_S$ and is always inside the PE region at $\sigma > \sigma_{\text{CEP}}$. Note that both wells $P_3 = 0$ and $P_3 = \pm P_S$ transform continuously into the one flat well in the BEP [see Figs. 2(b) and 2(c)].

As it follows from Eqs. (1b) and (1d), the critical temperature T_{cr} of the PE phase instability is determined from the equation $\frac{1}{2}\alpha^*(T_{\text{cr}}, \zeta, \Lambda) - \sigma_i Q_{i3} - W_{ij3}\sigma_i\sigma_j = 0$, where the coefficient $\alpha^*(T_{\text{cr}}, \zeta, \Lambda)$ is given by Eq. (2). As illustrated below, the screening factor Λ, the shape factor ζ, and the elastic stresses σ_i can strongly change the value of T_{cr} and consequently can influence the polar properties of the core at the working temperature. Since different shapes of core-shell nanoparticles are of interest for fundamental research and applications, the influence of the screening factor Λ on their phase diagrams and polar properties is illustrated in Figs. 3–6 for nanoparticles with various shape factors ζ under different pressures σ.

Phase diagrams of the core-shell CIPS nanoparticles as a function of both shape (ζ) and screening (Λ) factors are shown in Fig. 3 for several temperatures over the range 100–300 K. The diagrams (a)–(f) correspond to different values of hydrostatic pressure σ varying in the range -300 MPa $\leqslant \sigma \leqslant 200$ MPa. Note that the changes between the diagrams (a)–(f) are pressure induced. The absence of red curves in the diagrams (c)–(f) means that the nanoparticle is in the PE phase at 300 K and $\sigma \leqslant 0$; the nanoparticle cannot be in the FI phase because $T_{\text{cr}} < 0$ K for the negative pressures in the considered ranges of screening and shape factors (simply meaning that
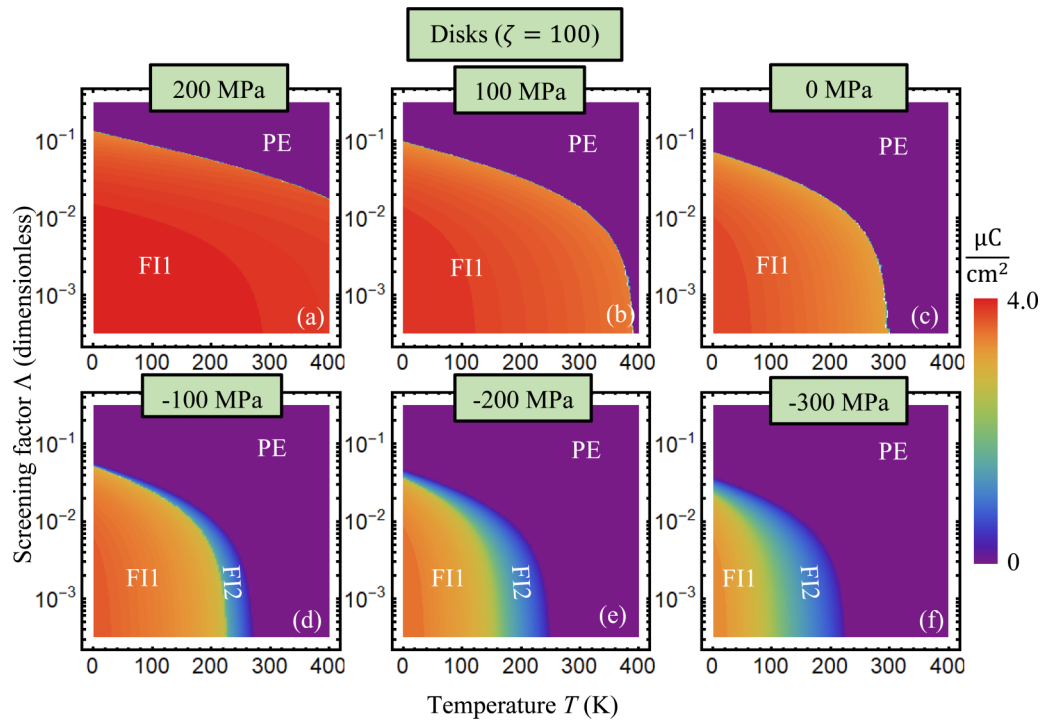
FIG. 4. The dependence of the spontaneous polarization P_3 on the temperature T and screening factor Λ calculated for core-shell nanodisks (shape factor $\zeta = 100$) at different hydrostatic pressures (a) $\sigma = 200$ MPa, (b) 100 MPa, (c) 0 MPa, (d) -100 MPa, (e) -200 MPa, and (f) -300 MPa. The polarization vector is perpendicular to the disk surface.

there is no FI-PE phase transition at $T \geqslant 0$ K). Similarly, the absence of a magenta curve in the diagram (f) means that the nanoparticle is in the PE phase at 250 K and $\sigma \leqslant -300$ MPa. At the temperatures <200 K, the core-shell nanoparticles can be in the FE phase for -300 MPa $\leqslant \sigma \leqslant 200$ MPa [see blue, green, and black curves in the diagrams (a)–(f)].

The common feature of the diagrams, shown in Fig. 3, is that the FI-PE transition temperature and the area of the FI phase increases for the case of compression $\sigma > 0$ and decreases for the case of tension $\sigma < 0$ [compare the position of red, magenta, and blue curves in the diagrams (a)–(f)]. This trend is opposite to the situation observed for many uniaxial and multiaxial perovskite nanoparticles, where the FI-PE transition temperature and the area of the FI phase increases for negative hydrostatic pressure. The origin of this difference is the negative nonlinear electrostriction couplings $Z_{i33} < 0$ and $W_{ij33} < 0$ and the inverted signs of the linear electrostriction coupling $Q_{33} < 0$, $Q_{23} > 0$, and $Q_{13} > 0$ (see Table I).

The PE phase, located in the top right part of the diagrams, enlarges its area with an increase in Λ and/or ζ, meaning that the phase stability increases with an increase in the screening factor (e.g., for semiconducting shells with $\Lambda > 0.1$), as well as with a decrease of the core length in the polarization direction (e.g., for spherical or oblate ellipsoidal cores with $\zeta \geqslant 1$). The FI phase, located in the bottom left part of the diagrams, enlarges its area with a decrease in Λ and/or ζ, meaning that the phase stability increases with a decrease in the screening factor (e.g., for conducting shells with $\Lambda < 0.01$), as well as with an increase of the core length in the polarization direction (e.g., for prolate ellipsoidal cores with $\zeta < 1$). As anticipated,

the area of the PE phase decreases and the area of the FI phase increases with a decrease in temperature (compare the position of different curves in the diagrams).

Another common feature of great importance in the diagrams shown in Fig. 3 is their strong dependence on the screening factor Λ. Namely, the curves of the FI-PE phase transition have nearly vertical regions, which indicate a screening-induced nature of the transition. The transition occurs at a critical value of the screening length $\Lambda = \Lambda_{cr}(\zeta, T, \sigma)$, which depends on the temperature and pressure. The screening-induced FI-PE transition is caused by the depolarization energy contribution, whose strength is determined by the Λ value. Thus, the tunable screening shell is responsible for inducing, maintaining, or destroying the polar state in the nanoparticle core.

The dependence of the spontaneous polarization P_3 on both temperature T and screening factor Λ, calculated for core-shell CIPS nanodisks (shape factor $\zeta = 100$), nanospheres (shape factor $\zeta = 1$), and nanoneedles (shape factor $\zeta = 0.1$), is shown in Figs. 4–6, respectively. Color maps (a)–(f) correspond to different values of hydrostatic pressure σ varying in the range -300 MPa $\leqslant \sigma \leqslant 200$ MPa. The polarization vector is perpendicular to the disk surface in Fig. 4 and is pointed along the needle's long axis in Fig. 6.

The maps (a)–(c), calculated for positive and zero pressures σ, contain a large reddish FI1 region with a relatively large polarization P_3 that has a sharp boundary with the violet PE region with zero P_3. The sharpness of the FI-PE boundary corresponds to a first-order phase transition. The area of the FI1 state with a large P_3 decreases with a decrease in σ [compare the maps (a)–(c)]. The maps (d)–(f), calculated for negative
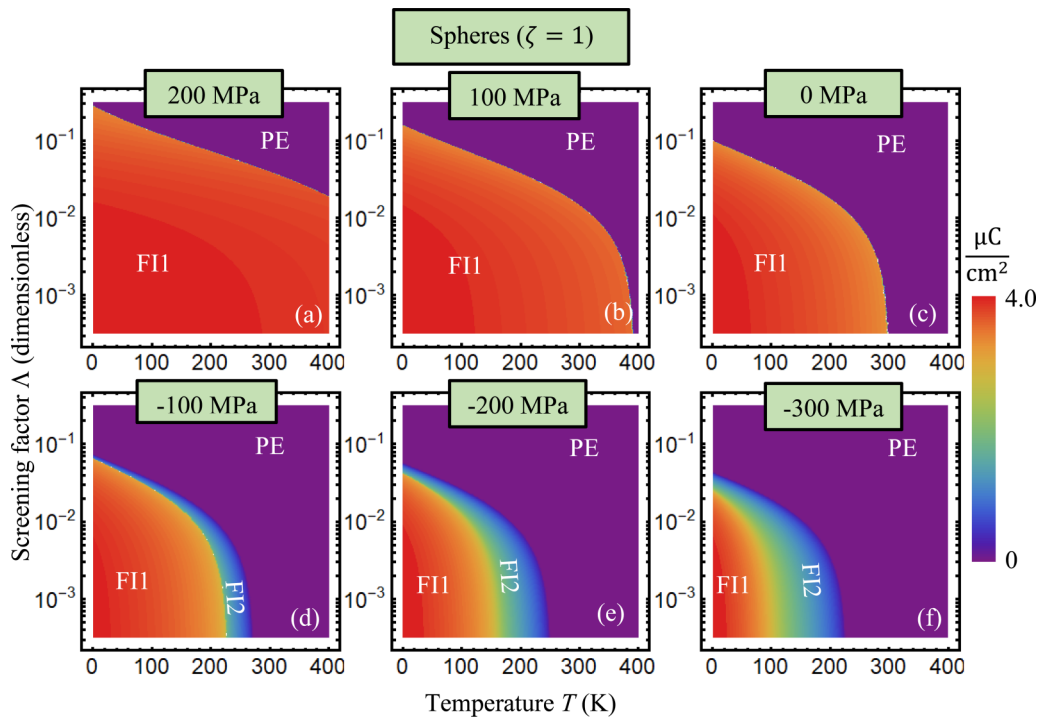
FIG. 5. The dependence of the spontaneous polarization P_3 on the temperature T and screening factor Λ calculated for core-shell nanospheres (shape factor $\zeta = 1$) at different hydrostatic pressures: (a) $\sigma = 200$ MPa, (b) 100 MPa, (c) 0 MPa, (d) -100 MPa, (e) -200 MPa, and (f) -300 MPa.

pressures σ, contain significantly smaller FI1 regions of a moderate polarization P_3 that has a diffuse boundary with the FI2 region of a small P_3. The FI region also borders with the

PE region of zero P_3. The diffuseness of the FI1-FI2 and FI2-PE boundaries corresponds to a second-order phase transition. The diffuse area of the FI2 state significantly enlarges with the
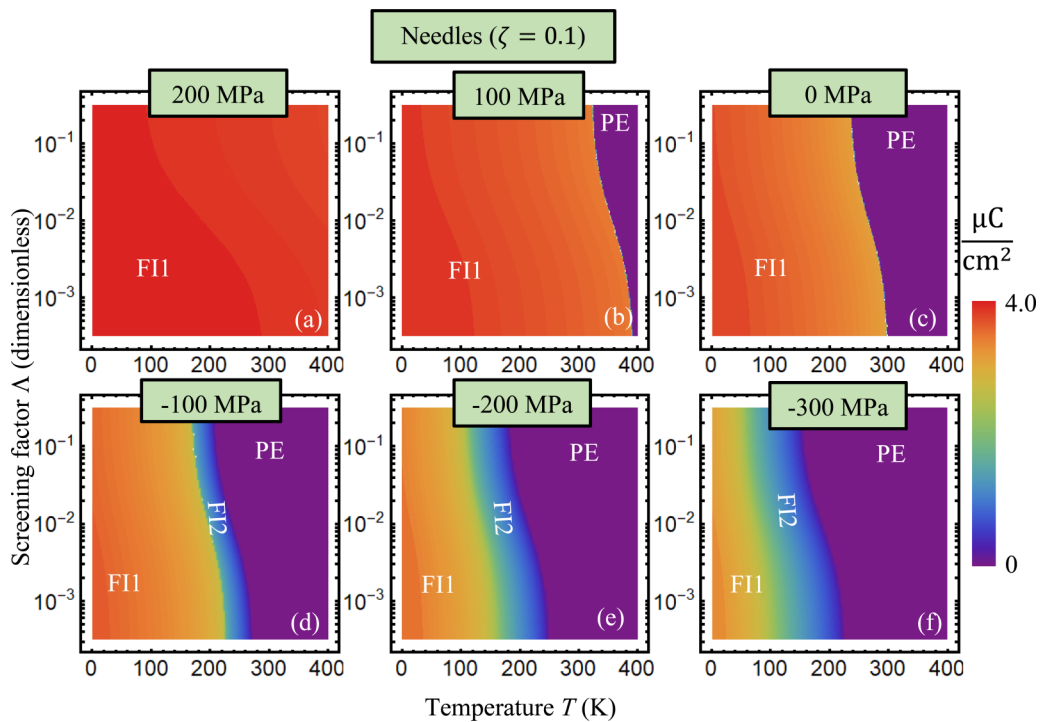

FIG. 6. The dependence of the spontaneous polarization P_3 on the temperature T and screening factor Λ calculated for core-shell nanoneedles (shape factor $\zeta = 0.1$) at different hydrostatic pressures (a) $\sigma = 200$ MPa, (b) 100 MPa, (c) 0 MPa, (d) -100 MPa, (e) -200 MPa, and (f) -300 MPa. The polarization vector is along the needle axis.

increase in the magnitude of negative pressure [compare the maps (d)–(f) for $\sigma < 0$].

The area of the FI1 state varies significantly as a function of the nanoparticle shape. This area is smallest for nanodisks (see Fig. 4), becomes very slightly larger for nanospheres (for which the polarization magnitude is greater), especially for $\sigma < 0$ (see Fig. 5), and significantly larger for nanoneedles (see Fig. 6); in this latter case, it can fill the entire map for $\sigma > 150$ MPa [see Fig. 6(a)]. The shape-dependent changes of the FI1 state area and the corresponding changes of polarization are caused by the depolarization field contribution, which is proportional to the depolarization factor [1,2]. The depolarization factor n_d, given by Eq. (3), is greatest for nanodisks with $\zeta \gg 1$ (with the polarization vector perpendicular to the disk surface), moderate for nanospheres, and decreases as $\frac{1}{\zeta}$ for nanoneedles with $\zeta \ll 1$ (with the polarization vector pointed along the needle long axis; see Appendix B). The relative area of the FI2 state with small P_3, which exists for negative σ, is approximately the same for nanodisks, nanospheres, and nanoneedles [compare, e.g., Figs. 4(f), 5(f), and 6(f)]. The area of the PE phase without a spontaneous polarization is the largest for nanodisks (see Fig. 4), slightly less for nanospheres (see Fig. 5), and significantly smaller for nanoneedles (see Fig. 6), where for the latter case is absent if $\sigma > 150$ MPa [see Fig. 6(a)]. Note that the shape of the FI-PE boundary (either a sharp, first-order transition for $\sigma \geqslant 0$ or a diffuse, second-order transition for $\sigma < 0$) is similar for the nanodisks and nanospheres, being close to a parabolic curve with a rather small slope followed by a nearly vertical drop for $\sigma \leqslant 100$ MPa, whereas the shape of the boundary for the nanoneedles is close to a meander with two rather steep slopes. This drastic difference originated from the specific dependence of the depolarization factor n_d on the shape factor ζ.

The common feature of the spontaneous polarization color maps, shown in Figs. 4–6, is their significant dependence on the screening factor Λ. The screening controls the polarization value, especially in the FI1 state with large P_3 values, whose sharp boundary strongly depends on Λ and weakly depends on the temperature T. The screening role becomes a little weaker with the decrease in P_3, e.g., in the FI2 state with a small P_3 whose diffuse boundaries depend on T and σ. The impact of the screening factor on P_3 is caused by the depolarization field, where the magnitude of the screening is proportional to the Λ value; therefore, the tunable screening shell is responsible for inducing, maintaining, or destroying the spontaneous polarization of the nanoparticle core.

An important note to make is that phase diagrams and transition orders depend on pressure for many ferroics. The physical origin of the dependence is the electrostriction coupling. The order changes if the coupling renormalizes higher coefficients in LGD free energy. Since CIPS provides a negative nonlinear electrostriction, unlike most other ferroelectric materials, this condition (i.e., negative components $Z_{i33} < 0$ and $W_{ij3} < 0$) gives us a second-order FI-PE transition for the case of negative pressures.

Analytical results, discussed above, are based on the analytical expressions in Eq. (3) for the depolarization factors, which are only available for the ellipsoidal shape particle. However, despite significant technological advances, it is still rather difficult to synthesize ultra-small ferroic nanoparticles with the minimal size 5 nm or less while maintaining a fully controllable shape. It is a big challenge to make high-quality ensembles of perovskite, ternary oxide, and especially van der Waals layered chalcogenide nanoparticles in the form of regular ellipsoids with a controllable aspect ratio.

At the same time, it is quite possible to synthesize multi-layer CIPS nanoflakes and control the height of the flake by changing the number of layers [50]. From a theoretical standpoint, the CIPS nanoflake with a height $h = 10$ nm or more and a much bigger average lateral size L can be substituted by a disk-shape nanoparticle and considered within a continuous media approximation. Numerical simulations show that the accuracy of such an approximation is rather high—not less than several percent—because the effects related to irregular lateral edges of the nanoflake become insignificant for $L > 10 h$.

It also can be possible to make nanowires and/or nanotubes by curling CIPS layers/nanoflakes and controlling their radius and number of layers (like one creates and controls the sizes of carbon nanotubes). From a theoretical standpoint, the nanorod with a radius $R = 10$ nm or more and a much greater length L can be substituted by a needle-shaped ellipsoid and considered within a continuous media approximation with the accuracy not less than several percent because the effects related to nanowire vertical ends become insignificant for $L > 10 R$.

It is hardly possible to make spherical CIPS nanoparticles, but it is quite possible to grind multilayer nanoflakes or a bulk CIPS using, e.g., ball milling, and then to separate the milled particles by average sizes using nanoporous sieves. From this, one can obtain ensembles of nanoslices of irregular shape and the same average size (or sizes). From a theoretical standpoint, the average size (or sizes) becomes an effective radius (or sizes) of a spherical (or ellipsoidal) nanoparticle. The accuracy of such a substitution can be high or low depending on the scattering of sizes and shapes in the ensemble, but it is the only way to obtain analytical results using an effective media approach. The covering of a CIPS nanoparticle by a shell is a much simpler technological task in comparison with their sintering, and the cover typically smooths the sharp edges of the nanoparticles.

V. CONCLUSIONS

Using the LGD approach, we study screening-induced phase transitions in core-shell nanoparticles as a function of the particle shape: an oblate disk, a sphere, and a prolate needle. The nanoparticle core is made of a ferroic CIPS and covered by a tunable screening shell made of a phase-change material whose conductivity varies between semiconductor and metallic states. We revealed a very strong influence of the screening shell on the phase diagrams and polar properties of the nanoparticles.

The curves of FI-PE phase transition depend strongly on the screening factor Λ, which indicates a screening-induced nature of the transition. The transition occurs at some critical value of the screening length, which depends on the nanoparticle shape, temperature, and pressure. An important common feature is that phase transition order depends on pressure due to the electrostriction coupling. The order changes if the coupling renormalizes higher coefficients in LGD free energy.

Since CIPS provides a negative nonlinear electrostriction, unlike most other ferroelectric materials, this condition (i.e., negative components Z_{i33} and W_{ij3}) gives us a second-order FI-PE transition for the case of negative pressures $\sigma < \sigma_{\text{CEP}}$.

The screening-induced FI-PE transition is caused by the depolarization energy contribution, where its strength is determined by the screening length. The FI phase has two states, FI1 and FI2, whose properties are screening sensitive. The screening also controls the spontaneous polarization P_3, especially in the FI1 state with a large P_3, where the sharp boundary strongly depends on Λ. The screening effect becomes slightly weaker in the FI2 state with a small P_3, where its diffuse boundaries strongly depend on the temperature and pressure. The screening impact on P_3 is caused by the depolarization field, where its strength is proportional to the Λ value.

If the FI1 and FI2 states, predicted theoretically, exist in real CIPS nanoparticles, they should coexist when their potential energies differ in value by an amount less than the thermal energy. Since the potential barrier between the close-energy FI1 and FI2 states can exist [e.g., at the temperatures between the black and dark-violet curves in Fig. 2(b)], the regions with the small and large P_3 can be randomly mixed in the nanoparticle core. The mixture can be interpreted as the spatially inhomogeneous quasirandom polar phase. The switchable energy-degenerated FI1 and FI2 states can be promising candidates for multibits and high-T qubits. Since the tunable screening shell is responsible for inducing, maintaining, or destroying the polar state in the nanoparticle core, the results obtained in this paper can be of particular interest for core-shell nanoparticles applications in nonvolatile memory cells.

APPENDIX A

If one considers observable (i.e., measurable) polar displacements only, P_3 is a proper candidate for a ferroelectric order parameter. Any FI (antiferroelectric or ferrimagnetic) material has two (or more) polar (or magnetic) sublattices, where electric (or magnetic) dipole moments are aligned antiparallel. Therefore, corresponding phenomenological models must consider at least two order parameters as independent variables, which are, e.g., the sum and the difference of the sublattice dipole moments in the Kittel-type models. As a rule, the antipolar and antiferromagnetic order parameters cannot

be directly measured. Since $CuInP_2(S, Se)_6$ is a FI (not ferroelectric) material (see, e.g., Refs. [13,51,52]), we must also consider the antipolar order parameter.

Hence, a conventional expansion of a FI Landau-Devonshire thermodynamic potential contains even powers (2, 4, and 6) of the polar and antipolar order parameters P_3 and A_3 and the biquadratic coupling between them. Due to the need to describe the first-order phase transitions, we cannot cut the expansion on the fourth powers of P_3 and A_3; therefore, the expansion includes the sixth powers of P_3 and A_3. The corresponding expansion is

$$G[P_3, A_3] = \frac{a}{2}P_3^2 + \frac{b}{4}P_3^4 + \frac{c}{6}P_3^6 - P_3 E_3 + \frac{d}{2}A_3^2 P_3^2 + \frac{f}{2}A_3^2$$
$$+ \frac{g}{4}A_3^4 + \frac{h}{6}A_3^6. \quad \text{(A1)}$$

Here, a, b, c, d, f, g, and h are expansion coefficients, and E_3 is an electric field. Minimization of $G[P_3, A_3]$ with respect to A_3 yields

$$\frac{\partial G}{\partial A_3} = A_3(dP_3^2 + f) + gA_3^3 + hA_3^5. \quad \text{(A2)}$$

The solutions of equation $\frac{\partial G}{\partial A_3} = 0$ are $A_3 = 0$ and $A_3^2 = \frac{-g \pm \sqrt{g^2 - 4fh - 4dhP_3^2}}{2h}$. Substituting the nonzero solution for A_3^2 in Eq. (A1), after algebraic transformations and serial expansion on P_3^2 and further omitting highest order expansion terms proportional to P_3^{10} and P_3^{12}, we obtain

$$g_{\text{LD}}[P_3, A_3] = \frac{\alpha}{2}P_3^2 + \frac{\beta}{4}P_3^4 + \frac{\gamma}{6}P_3^6 + \frac{\delta}{8}P_3^8 - P_3 E_3, \quad \text{(A3)}$$

where $\alpha \sim a$, $\beta \sim b$, $\gamma \sim c$, and $\delta \sim \frac{d^4 h^2}{g^5}$. Thus, we can conclude that the biquadratic coupling term between the order parameters $\frac{d}{2}A_3^2 P_3^2$ induces the term $\frac{\delta}{8}P_3^8$ in Eq. (A3).

APPENDIX B

Most of the essential changes of the depolarization factor n_d appear when the shape factor changes from very small values ($\zeta = \frac{R}{L} \ll 1$, needles) to larger values ($\zeta = 1 - 3$, sphere and spherelike; see Fig. 7). There is a saturation curve at $\zeta > 5$ when n_d becomes close to unity and weakly independent on ζ for disklike nanoparticles. The depolarization factor controls the transition temperature in accordance with Eq. (2); this means that, for oblate nanoparticles (i.e., for disklike), their shape becomes less important than other factors, such as temperature, pressure, and of course, screening length Λ. Note that the screening length Λ is included in the depolarization factor $\frac{n_d}{\varepsilon_0[\varepsilon_b n_d + \varepsilon_e(1-n_d) + n_d \Lambda]}$:

$$\alpha^*(T, n_d, \Lambda) = \alpha(T) + \frac{n_d}{\varepsilon_0[\varepsilon_b n_d + \varepsilon_e(1-n_d) + n_d \Lambda]}. \quad \text{(B1)}$$

The depolarization factor controls the critical temperature in accordance with equation $\frac{1}{2}\alpha^*(T_{\text{cr}}, n_d, \Lambda) - \sigma_i Q_{i3} - W_{ij3}\sigma_i \sigma_j = 0$; when n_d is very small (for needles), $n_d \Lambda$ is also small, and so the phase boundaries in Fig. 6 become more vertical, meaning that they are much more temperature dependent than the case shown in Fig. 4.
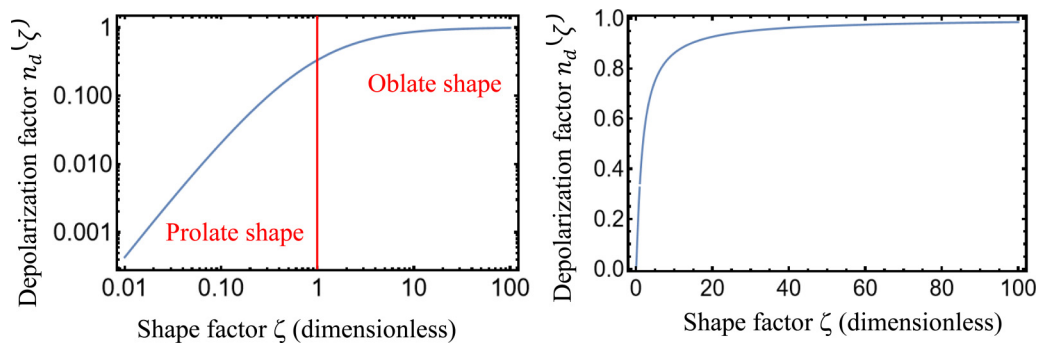
FIG. 7. The dependence of the depolarization factor $n_d(\zeta)$ on the shape factor $\zeta = \frac{R}{L}$ plotted in log-log scale (left) and linear scale (right).

[1] A. N. Morozovska, E. A. Eliseev, and M. D. Glinchuk, Ferroelectricity enhancement in confined nanorods: Direct variational method, Phys. Rev. B **73**, 214106 (2006).

[2] A. N. Morozovska, M. D. Glinchuk, and E. A. Eliseev, Phase transitions induced by confinement of ferroic nanoparticles, Phys. Rev. B **76**, 014102 (2007).

[3] S. V. Kalinin, Y. Kim, D. Fong, and A. N. Morozovska, Surface-screening mechanisms in ferroelectric thin films and their effect on polarization dynamics and domain structures, Rep. Prog. Phys. **81**, 036502 (2018).

[4] A. N. Morozovska, E. A. Eliseev, S. V. Kalinin, and R. Hertel, Flexo-sensitive polarization vortices in thin ferroelectric films, Phys. Rev. B **104**, 085420 (2021).

[5] X. Bourdon, V. Maisonneuve, V. B. Cajipe, C. Payen, and J. E. Fischer, Copper sublattice ordering in layered $CuMP_2Se_6$ ($M =$ In, Cr), J. All. Comp. **283**, 122 (1999).

[6] A. Belianinov, Q. He, A. Dziaugys, P. Maksymovych, E. Eliseev, A. Borisevich, A. Morozovska, J. Banys, Y. Vysochanskii, and S. V. Kalinin, $CuInP_2S_6$ room temperature layered ferroelectric, Nano Lett. **15**, 3808 (2015).

[7] M. A. Susner, M. Chyasnavichyus, M. A. McGuire, P. Ganesh, and P. Maksymovych, Metal thio- and selenophosphates as multifunctional van der Waals layered materials, Adv. Mater. **29**, 1602852 (2017).

[8] M. Wu and P. Jena, The rise of two-dimensional van der Waals ferroelectrics, WIREs Comput. Mol. Sci. **8**, e1365 (2018).

[9] F. Liu, L. You, K. L. Seyler, X. Li, P. Yu, J. Lin, X. Wang, J. Zhou, H. Wang, H. He *et al.*, Room-temperature ferroelectricity in $CuInP_2S_6$ ultrathin flakes, Nat. Commun. **7**, 12357 (2016).

[10] M. A. Susner, M. Chyasnavichyus, A. A. Puretzky, Q. He, B. S. Conner, Y. Ren, D. A. Cullen, P. Ganesh, D. Shin, H. Demir *et al.*, Cation-eutectic transition via sublattice melting in $CuInP_2S_6/In_{4/3}P_2S_6$ van der Waals layered crystals, ACS Nano **11**, 7060 (2017).

[11] M. Osada and T. Sasaki, The rise of 2D dielectrics/ferroelectrics, APL Mater. **7**, 120902 (2019).

[12] C. Chen, H. Liu, Q. Lai, X. Mao, J. Fu, Z. Fu, and H. Zeng, Large-scale domain engineering in two-dimensional ferroelectric $CuInP_2S_6$ via giant flexoelectric effect, Nano Lett. **22**, 3275 (2022).

[13] V. Maisonneuve, V. B. Cajipe, A. Simon, R. Von Der Muhll, and J. Ravez, Ferrielectric ordering in lamellar $CuInP_2S_6$, Phys. Rev. B **56**, 10860 (1997).

[14] P. Toledano and M. Guennou, Theory of antiferroelectric phase transitions, Phys. Rev. B **94**, 014107 (2016).

[15] J. A. Brehm, S. M. Neumayer, L. Tao, A. O'Hara, M. Chyasnavichus, M. A. Susner, M. A. McGuire, S. V. Kalinin, S. Jesse, P. Ganesh *et al.*, Tunable quadruple-well ferroelectric van der Waals crystals, Nat. Mater. **19**, 43 (2020).

[16] W. Song, R. Fei, and L. Yang, Off-plane polarization ordering in metal chalcogen diphosphates from bulk to monolayer, Phys. Rev. B **96**, 235420 (2017).

[17] Yu. M. Vysochanskii, A. A. Molnar, M. I. Gurzan, V. B. Cajipe, and X. Bourdon, Dielectric measurement study of lamellar $CuInP_2Se_6$: Successive transitions towards a ferroelectric state via an incommensurate phase? Sol. State Comm. **115**, 13 (2000).

[18] V. Liubachko, V. Shvalya, A. Oleaga, A. Salazar, A. Kohutych, A. Pogodin, and Yu. M. Vysochanskii, Anisotropic thermal properties and ferroelectric phase transitions in layered $CuInP_2S_6$ and $CuInP_2Se_6$ crystals, J. Phys. Chem. Sol. **111**, 324 (2017).

[19] A. Dziaugys, I. Zamaraite, J. Macutkevic, D. Jablonskas, S. Miga, J. Dec, Yu. Vysochanskii, and J. Banys, Non-linear dielectric response of layered $CuInP_2S_6$ and $Cu_{0.9}Ag_{0.1}InP_2S_6$ crystals, Ferroelectrics **569**, 280 (2020).

[20] V. Samulionis, J. Banys, and Yu. Vysochanskii, Linear and nonlinear elastic properties of $CuInP_2S_6$ layered crystals under polarization reversal, Ferroelectrics **389**, 18 (2009).

[21] J. Banys, J. Macutkevic, V. Samulionis, A. Brilingas, and Yu. Vysochanskii, Dielectric and ultrasonic investigation of phase transition in $CuInP_2S_6$ crystals, Ph. Transit. **77**, 345 (2004).

[22] S. M. Neumayer, E. A. Eliseev, M. A. Susner, B. J. Rodriguez, S. Jesse, S. V. Kalinin, M. A. McGuire, A. N. Morozovska, P. Maksymovych, and N. Balke, Giant negative electrostriction and dielectric tunability in a van der Waals layered ferroelectric, Phys. Rev. Mater. **3**, 024401 (2019).

[23] V. Samulionis, J. Banys, and Yu. Vysochanskii, Piezoelectric and ultrasonic studies of mixed $CuInP_2(S_xSe_{1-x})_6$ layered crystals, Ferroelectrics **351**, 88 (2007).

[24] Yu. Vysochanskii, R. Yevych, L. Beley, V. Stephanovich, V. Mytrovcij, O. Mykajlo, A. Molnar, and M. Gurzan, Phonon spectra and phase transitions in $CuInP_2(Se_xS_{1-x})_6$ ferroelectrics, Ferroelectrics **284**, 161 (2003).

[25] A. Dziaugys, K. Kelley, J. A. Brehm, L. Tao, A. Puretzky, T. Feng, A. O'Hara, S. Neumayer, M. Chyasnavichyus, E.

A. Eliseev *et al.*, Piezoelectric domain walls in van der Waals antiferroelectric $CuInP_2Se_6$, Nat. Commun. **11**, 3623 (2020).

[26] A. N. Morozovska, E. A. Eliseev, K. Kelley, Yu. M. Vysochanskii, S. V. Kalinin, and P. Maksymovych, Phenomenological description of bright domain walls in ferroelectric-antiferroelectric layered chalcogenides, Phys. Rev. B **102**, 174108 (2020).

[27] A. N. Morozovska, E. A. Eliseev, S. V. Kalinin, Y. M. Vysochanskii, and Petro Maksymovych, Stress-induced phase transitions in nanoscale $CuInP_2S_6$, Phys. Rev. B **104**, 054102 (2021).

[28] E. A. Eliseev, Y. M. Fomichov, S. V. Kalinin, Yu. M. Vysochanskii, P. Maksymovich, and A. N. Morozovska, Labyrinthine domains in ferroelectric nanoparticles: manifestation of a gradient-induced morphological phase transition, Phys. Rev. B **98**, 054101 (2018).

[29] A. N. Morozovska, Y. M. Fomichov, P. Maksymovych, Yu. M. Vysochanskii, and E. A. Eliseev, Analytical description of domain morphology and phase diagrams of ferroelectric nanoparticles, Acta Mater. **160**, 109 (2018).

[30] A. N. Morozovska, E. A. Eliseev, Y. M. Fomichov, Yu. M. Vysochanskii, V. Yu. Reshetnyak, and D. R. Evans, Controlling the domain structure of ferroelectric nanoparticles using tunable shells, Acta Mater. **183**, 36 (2020).

[31] A. N. Morozovska, E. A. Eliseev, R. Hertel, Y. M. Fomichov, V. Tulaidan, V. Yu. Reshetnyak, and D. R. Evans, Electric field control of three-dimensional vortex states in core-shell ferroelectric nanoparticles, Acta Mater. **200**, 256 (2020).

[32] E. A. Eliseev, A. N. Morozovska, R. Hertel, H. V. Shevliakova, Y. M. Fomichov, V. Yu. Reshetnyak, and D. R. Evans, Flexo-elastic control factors of domain morphology in core-shell ferroelectric nanoparticles: Soft and rigid shells, Acta Mater. **212**, 116889 (2021).

[33] A. N. Morozovska, R. Hertel, S. Cherifi-Hertel, V. Yu. Reshetnyak, E. A. Eliseev, and D. R. Evans, Chiral polarization textures induced by the flexoelectric effect in ferroelectric nanocylinders, Phys. Rev. B **104**, 054118 (2021).

[34] A. N. Morozovska, E. A. Eliseev, S. Cherifi-Hertel, D. R. Evans, and R. Hertel, Electric field control of labyrinthine domain structures in core-shell ferroelectric nanoparticles, Phys. Rev. B **106**, 144104 (2022).

[35] N. A. Pertsev, A. G. Zembilgotov, and A. K. Tagantsev, Effect of Mechanical Boundary Conditions on Phase Diagrams of Epitaxial Ferroelectric Thin Films, Phys. Rev. Lett. **80**, 1988 (1998).

[36] Yu. M. Vysochanskii, M. M. Mayor, V. M. Rizak, V. Yu. Slivka, and M. M. Khoma, The tricritical Lifshitz point on the phase diagram of $Sn_2P_2(Se_xS_{1-x})_6$, Sov. JETP **95**, 1355 (1989).

[37] A. Kohutych, R. Yevych, S. Perechinskii, V. Samulionis, J. Banys, and Yu. Vysochanskii, Sound behavior near the Lifshitz point in proper ferroelectrics, Phys. Rev. B **82**, 054101 (2010).

[38] A. N. Morozovska, I. S. Golovina, S. V. Lemishko, A. A. Andriiko, S. A. Khainakov, and E. A. Eliseev, Effect of Vegard strains on the extrinsic size effects in ferroelectric nanoparticles, Phys. Rev. B **90**, 214103 (2014).

[39] E. A. Eliseev, A. V. Semchenko, Y. M. Fomichov, M. D. Glinchuk, V. V. Sidsky, V. V. Kolos, Yu. M. Pleskachevsky, M. V. Silibin, N. V. Morozovsky, and A. N. Morozovska, Surface and finite size effects impact on the phase diagrams, polar and dielectric properties of $(Sr,Bi)Ta_2O_9$ ferroelectric nanoparticles, J. Appl. Phys. **119**, 204104 (2016).

[40] L. D. Landau, E. M. Lifshitz, and L. P. Pitaevskii, *Electrodynamics of Continuous Media*, 2nd ed. (Butterworth-Heinemann, Oxford, 1984).

[41] A. K. Tagantsev and G. Gerra, Interface-induced phenomena in polarization response of ferroelectric thin films, J. Appl. Phys. **100**, 051607 (2006).

[42] P. Guranich, V. Shusta, E. Gerzanich, A. Slivka, I. Kuritsa, and O. Gomonnai, Influence of hydrostatic pressure on the dielectric properties of $CuInP_2S_6$ and $CuInP_2Se_6$ layered crystals, J. Phys. Conf. Ser. **79**, 012009 (2007).

[43] A. V. Shusta, A. G. Slivka, V. M. Kedylich, P. P. Guranich, V. S. Shusta, E. I. Gerzanich, and I. P. Prits, Effect of uniaxial pressure on dielectric properties of $CuInP_2S_6$ crystals, Sci. Herald Uzhhorod University. Series Phys. **28**, 44 (2010).

[44] A. Molnar, K. Glukhov, M. Medulych, D. Gal, H. Ban, and Yu. Vysochanskii, The effect of changes in chemical composition and uniaxial compression on the phase transition of $CuInP_2S_6$ crystals, in *Abstract Book of the FMNT 2020 Online Conference* Virtual Vilnius, Lithuania (Vilnius University, Vilnius, 2020), pp. 23–26.

[45] V. Samulionis, J. Banys, Yu. Vysochanskii, and V. Cajipe, Elastic and electromechanical properties of new ferroelectric-semiconductor materials of $Sn_2P_2S_6$ family, Ferroelectrics **257**, 113 (2001).

[46] A. Kohutych, V. Liubachko, V. Hryts, Yu. Shiposh, M. Kundria, M. Medulych, K. Glukhov, R. Yevych, and Yu. Vysochanskii, Phonon spectra and phase transitions in van der Waals ferroics MM'P_2X_6, Mol. Cryst. Liq. Cryst. **747**, 14 (2022).

[47] https://www.wolfram.com/mathematica.

[48] https://notebookarchive.org/2022-12-2tkg52x.

[49] Sumedha and S. Mukherjee, Emergence of a bicritical end point in the random-crystal-field Blume-Capel model, Phys. Rev. E **101**, 042125 (2020).

[50] L. Chen, Y. Li, C. Li, H. Wang, Z. Han, He Ma, G. Yuan, L. Lin, Z. Yan, X. Jiang *et al.*, Thickness dependence of domain size in 2D ferroelectric $CuInP_2S_6$ nanoflakes, AIP Advances **9**, 115211 (2019).

[51] Y. M. Vysochanskii, V. A. Stephanovich, A. A. Molnar, V. B. Cajipe, and X. Bourdon, Raman spectroscopy study of the ferrielectric-paraelectric transition in layered $CuInP_2S_6$, Phys. Rev. B **58**, 9119 (1998).

[52] N. Sivadas, P. Doak, and P. Ganesh, Anharmonic stabilization of ferrielectricity in $CuInP_2Se_6$, Phys. Rev. Res. **4**, 013094 (2022).